



Ore component mobility, transport and mineralization at mid-oceanic ridges: A stable isotopes (Zn, Cu and Fe) study of the Rainbow massif (Mid-Atlantic Ridge 36°14'N)

B. Debret^{a,*}, H. Beunon^a, N. Mattielli^a, M. Andreani^b, I. Ribeiro da Costa^c, J. Escartin^d

^a Laboratoire G-Time, DGES, Université Libre de Bruxelles, ULB, CP 160/02, 1050, Brussels, Belgium

^b Université de Lyon, Université Claude Bernard Lyon 1, ENS de Lyon, CNRS, LGL-TPE, F-69622 Villeurbanne, France

^c Dept. de Geologia, Faculdade de Ciências, Universidade de Lisboa Edifício C6 – Piso 4, Campo Grande, 1749-016 Lisboa, Portugal

^d Institut de Physique du Globe de Paris, CNRS UMR 7154, Paris, France

ARTICLE INFO

Article history:

Received 11 May 2018

Received in revised form 6 September 2018

Accepted 7 September 2018

Available online 8 October 2018

Editor: D. Vance

Keywords:

hydrothermal deposits
stable isotopes
serpentinized peridotites
metals mobility

ABSTRACT

Ultramafic hosted hydrothermal deposits are ubiquitous along slow-spreading ridges such as the Mid-Atlantic Ridge (MAR; e.g., Ashadzé, Rainbow, Lost City) where they exert a major control on the cycling of economically important elements (e.g., Zn, Cu, Ni). However, the origin of metal mobility in these environments remains unclear. Here we use Zn ($\delta^{66}\text{Zn}$), Cu ($\delta^{65}\text{Cu}$) and Fe ($\delta^{56}\text{Fe}$) stable isotopes to explore the mobility of metals during (1) the serpentinization of the Rainbow massif basement in a seawater dominated system at low temperature (<250 °C) and (2) the subsequent high temperature (>350 °C) mineralization of serpentinites through seawater-derived fluids that interacted with gabbro prior to interacting with serpentinite near hydrothermal sites (stockworks).

The Rainbow samples display among the largest range of isotopic variations ever reported for ultramafic rocks ($-0.10\text{‰} \leq \delta^{66}\text{Zn} \leq +0.47\text{‰}$; $-0.93\text{‰} \leq \delta^{65}\text{Cu} \leq +0.24\text{‰}$; $-0.15\text{‰} \leq \delta^{56}\text{Fe} \leq +0.25\text{‰}$). These variations reflect a two-stage process. (1) Serpentinization of the ultramafic basement is accompanied by a decrease in Zn (26–41 ppm) and Cu (1–13 ppm) concentrations and an increase of $\delta^{66}\text{Zn}$ (+0.30–+0.47‰) in peridotites relative to primitive mantle (Zn ~ 55 ppm, Cu ~ 20 ppm, $\delta^{66}\text{Zn}$ ~ +0.16‰). Striking correlations between $\delta^{66}\text{Zn}$ and indices of serpentinization (LOI and $\text{Fe}^{3+}/\Sigma\text{Fe}$) show preferential leaching of isotopically light Zn by fluids during the serpentinization of the massif. This isotopic fractionation is controlled by the dissolution of both mantle sulfides and/or spinels and Zn complexation with chlorine in fluids. At this stage, Fe seems to be immobile as attested by correlations between $\delta^{56}\text{Fe}$ and indices of peridotite fertility (e.g., $\text{Al}_2\text{O}_3/\text{SiO}_2$). (2) The mineralization of serpentinites near the Rainbow stockwork is accompanied by an increase in $\text{Fe}^{3+}/\Sigma\text{Fe}$ (>0.7), FeO (up to 19.8 wt%), Zn (>>50 ppm) and Cu (>>20 ppm) concentrations. The $\delta^{66}\text{Zn}$ and $\delta^{65}\text{Cu}$ values progressively decrease with indices of serpentinite mineralization (e.g., Zn, Cu, $\text{Fe}^{3+}/\Sigma\text{Fe}$), while several samples display abnormally high $\delta^{56}\text{Fe}$ (up to 0.25‰) relative to primitive mantle ($\delta^{56}\text{Fe}$ ~ 0.025‰), suggesting a high mobility of Zn, Cu and Fe in high temperature hydrothermal fluids. These isotopic fractionations can be explained by the local oxidation of sulfur bearing fluids in contact with seawater. This process enhances metal precipitation as well as the formation of Fe^{3+} -bearing phases, such as magnetite, beneath the stockwork, explaining the presence of magnetic anomalies below the Rainbow hydrothermal field. Our study shows that the mobility of metals in hydrothermal fluids can be enhanced by both peridotite interaction with seawater or with fluid that interacted with deeper mafic bodies and then flowed to the surface. These processes may generate hydrothermal deposits with distinct metal signatures.

© 2018 Elsevier B.V. All rights reserved.

1. Introduction

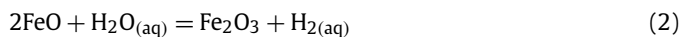
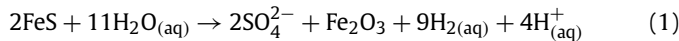
Hot, reducing (H_2 -rich) and metal-rich hydrothermal fluids that exit black smokers or carbonated chimneys at the seafloor can

* Corresponding author.

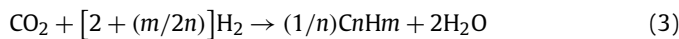
E-mail address: ba.debret@gmail.com (B. Debret).

be formed through interactions of seawater with oceanic mafic crust and/or its ultramafic basement. These interactions (1) modify the composition of oceanic lithosphere, (2) affect ocean chemistry, (3) produce metal-rich deposits (possible analogues to ore deposits present on land), and (4) sustain biological communities in the deep sea. Ultramafic hosted hydrothermal systems are commonly

observed along the slow-spreading Mid-Atlantic Ridge (MAR; e.g., Ashadzé, Rainbow, Logatchev, Lost City) and in several other places along ultraslow-spreading ridges (e.g., South West Indian Ridge or the Arctic Ridges), (meta-)ophiolites (e.g., New Caledonia; Bou Azzer paleo-hydrothermal system) or forearc basins (e.g., Marianas; Baker et al., 2004; Fouquet et al., 2010; Hodel et al., 2017; Kelley et al., 2001; Ohara et al., 2012). In those environments, the main H₂ production results from oxidation of primary S²⁻- or Fe²⁺-bearing phases to form sulfate-bearing serpentine (general equation (1); Debret et al., 2017) and Fe³⁺-bearing phases, such as magnetite at high temperature or Fe³⁺-serpentine at low temperature (general equation (2); Andreani et al., 2013; Bonnemains et al., 2016; Klein et al., 2014), respectively:



The reducing power of these general reactions has been recognized as a source for the production of abiotic hydrocarbons including methane via Fischer–Tropsch Type or Sabatier reactions, or of polyaromatic hydrocarbons (Holm and Charlou, 2001):



These environments are also associated with abundant sulfide deposits enriched in economically important elements such as Cu, Zn, Co, Au and Ni (e.g., Marques et al., 2007; Fouquet et al., 2010).

At slow- and ultraslow-spreading ridges, the source of metals in fluids remains unclear. It can arise from the interaction of circulating seawater with mantle peridotites and/or be an admixture of a fluid escaping from mafic bodies at depth. Indeed, the hydrothermal circulation within ultramafic rocks is generally related to low magmatic activity in which hydrothermal cells are likely driven by regional heat flow induced by ephemeral gabbroic intrusions cooling at depth and/or by exothermic heat produced during serpentinization (e.g., Allen and Seyfried, 2004; Dunn et al., 2017; Kelley et al., 2001). The latter is enhanced early during mantle exhumation by detachment faulting through the percolation of seawater dominated fluids. However, the nature and timing of the hydrothermal processes, the reaction pathways and/or the nature of the ligands that enhance metal mobility in ultramafic systems remain unknown.

Transition metal stable isotopes (e.g., Zn, Cu, Fe) provide key constraints on element mobility and mass balance, as equilibrium stable isotope fractionation between different phases (such as serpentine minerals, Fe-oxides, sulfides and fluids) is driven by contrasts in element bonding environment and oxidation state (e.g., Fujii et al., 2014). The mobility of Zn, Cu and Fe, and therefore isotopic fractionations of Zn, Cu and Fe isotopes, are particularly sensitive to chlorine, sulfur and/or carbon complexes in fluids. Those isotopic systems have the potential to provide new insights into metal mobility during fluid/rock interactions and to explore the origin of metal deposits in ultramafic systems. For example, Fe isotope values as low as -0.67‰ and as high as -0.09‰ have been measured in hydrothermal vent fluids along the MAR (e.g., Beard et al., 2003; Severmann et al., 2004), while associated hydrothermal deposits can display a large range of values (from about -2‰ to $+0.5\text{‰}$; e.g., Rouxel et al., 2008). Potential processes controlling the variability of isotopes in hydrothermal fluids and associated deposits include melt/rock interactions (e.g., Hedenquist and Lowenstern, 1994), metamorphism (e.g., Rouxel et al., 2003) and sub-seafloor processes leading to Fe precipitation or remobilization (e.g., Blanchard et al., 2009). However, studies of the effects of ore precipitation on isotopic systems are largely restricted to sulfide deposits and hydrothermal fluids (e.g., Beard et al., 2003; Rouxel

et al., 2008, 2004) while the ultramafic substratum, from which metals may have been extracted, is often neglected resulting in a major knowledge gap.

In this study we investigated Zn, Cu and Fe systematics of ultramafic rocks from the Rainbow massif ($36^\circ 14' \text{N}$), including rocks sampled near or at the hydrothermal field, and compared these results to other hydrothermal settings from slow- and ultraslow-spreading ridges and orogenic contexts. Among known hydrothermal areas, the Rainbow hydrothermal vent fluids are characterized by some of the highest H₂, CH₄ and metal (Fe, Mn, Cu, Zn and Co) concentrations ever reported (Charlou et al., 2002; Douville et al., 2002). The hydrothermal field is also associated with a positive magnetic anomaly (Szitkar et al., 2014), that is interpreted as the signature of a large-volume mineralized zone below the Rainbow hydrothermal field and likely corresponding to the stockwork. The Rainbow massif has also been the focus of recent geological and geophysical studies (Andreani et al., 2014; Dunn et al., 2017), that provide constraints on the structure and distribution of possible magma lenses and depth, and the location and geometry of the serpentinization front. Here we used stable isotopes to unravel the reaction pathway that produced hydrothermal fluids below venting areas for similar serpentinization systems at slow- and ultraslow-spreading ridges and provide a model of temporal and spatial variations of hydrothermal processes at depth, incorporating geological and geophysical constraints available.

2. Geological setting and sample selection

The Rainbow massif lies at $36^\circ 14' \text{N}$ along the MAR (Fig. 1) within a non-transform discontinuity. It is an inactive oceanic core complex (OCC) composed of peridotites intruded by gabbroic rocks and overlain by a sedimentary cover (Andreani et al., 2014; Canales et al., 2017). Seismic experiments have revealed the presence of numerous reflectors underlying the hydrothermal field and massif, at depths of 2–10 km, attributed to magma lenses variably crystallized (e.g., Canales et al., 2017). The massif also shows cone-shaped velocity gradient associated with seismic reflectors, where microseismicity concentrates, that are interpreted as the possible location of the serpentinization front (Dunn et al., 2017).

The massif hosts an active high temperature ($>350^\circ \text{C}$; Rainbow) and two inactive low temperature (serpentinization temperature inferior to 250°C ; Ghost City, Clamestone) hydrothermal sites (stockworks), near its summit at 2300 m water depth (Fig. 1), that were most probably established after the fault activity (Andreani et al., 2014). The active Rainbow field is located on the western flank of the massif and extends over $\sim 200 \times 100 \text{ m}$, heated by underlying magmatic bodies (Marques et al., 2006, 2007; Canales et al., 2017). This area is associated with a positive magnetic anomaly (Szitkar et al., 2014), which reflects the presence of a wide mineralized zone in the Rainbow stockwork, where several chemical processes concur to create and preserve strongly magnetized magnetite (e.g., Marques et al., 2006).

The dominant alteration of the massif was triggered by an early widespread and pervasive circulation of seawater-derived fluids during massif exhumation onto the seafloor. This episode was associated with the serpentinization of peridotites at temperatures ranging from 160 to 260°C (Andreani et al., 2014). Near the active venting area, petrographic observations reveal various stages of serpentinized peridotite recrystallization and sulfide precipitation (Andreani et al., 2014; Debret et al., 2017; Marques et al., 2006, 2007). Those are triggered by the circulation of high temperature ($\sim 360^\circ \text{C}$) and acidic ($\text{pH} \sim 3.5$) hydrothermal fluids (Charlou et al., 2002).

The studied samples were collected by dredging (DR-) and diving (PL-) during the FLORES (1996), SALDANHA (1998), IRIS (2001) and MoMARDREAM (2007, 2008) cruises (Fig. 1). Full descrip-

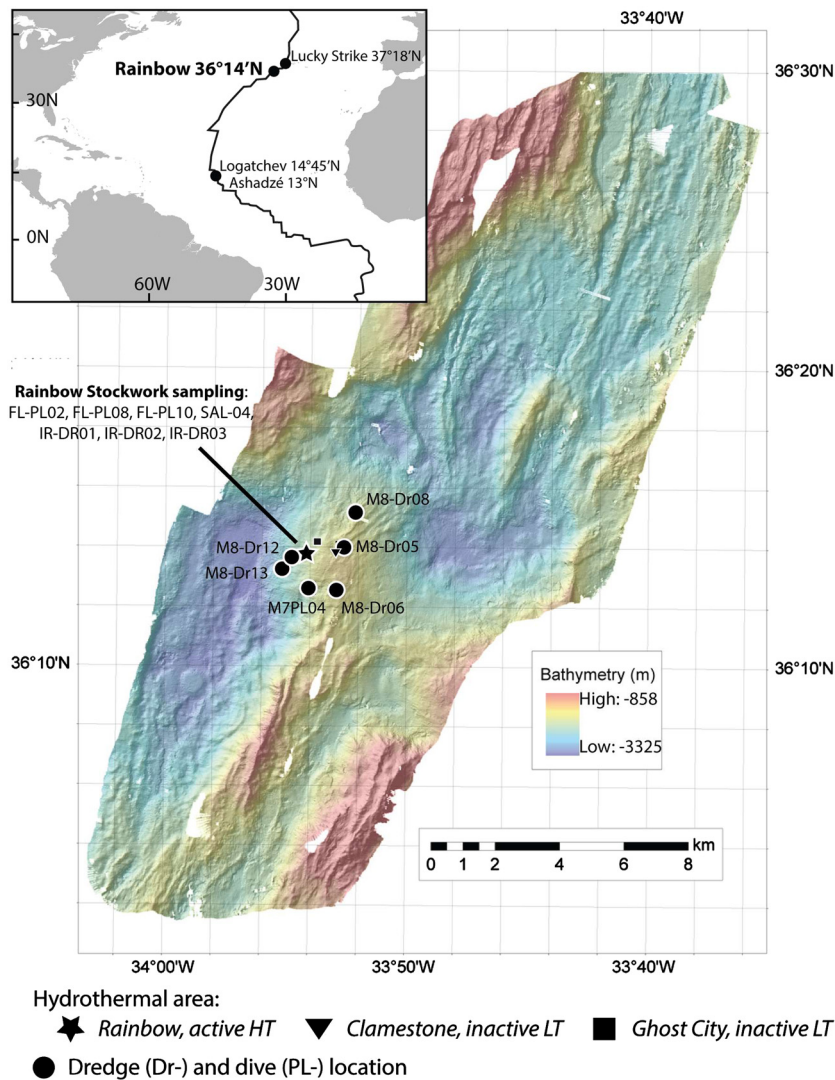


Fig. 1. Location of the dredging or diving sampling sites from the FLORES (FL), IRIS (IR) and MoMardream (M7 and M8) cruises. Most of the mineralized ultramafic rocks were sampled on the Rainbow active hydrothermal area with exception of M8-Dr12, M8-Dr13 and M8-Dr08 samples. Away from these zones, no evidence of mineralization of serpentinized peridotites has been observed (Andreani et al., 2014). Non-mineralized samples: M8-DR6-01a-c; M8-DR6-01a; M8-DR5-1; M7-PL04-14; M7-PL04-6; Mineralized samples: M8-Dr08-07a; M8-DR13-1A; M8-DR12-1a; M7-DR13-2; FL-PL10-15; SAL-04-01; IR-DR01-A-05; FL-PL02-04; IR-DR03-S; IR-DR02-L1; FL-PL08-05). HT: High temperature; LT: Low temperature.

tions of the studied samples are available elsewhere (Ribeiro da Costa, 2005; Marques et al., 2006, 2007; Andreani et al., 2014; Debret et al., 2017). Two different kinds of samples have been studied (Appendix A). (1) The first group of samples was recovered away from the Rainbow stockwork (Fig. 1). These samples correspond to non-mineralized pseudomorphic serpentinites. The serpentinization degree of the samples is high (typically higher than 80%) with, sometimes, olivine and orthopyroxene embedded within mesh and bastite textures, respectively, associated with thin strings of magnetite and crosscut by late chrysotile veins. Mantle Cr-spinel is usually partly recrystallized to ferritchromite and/or magnetite (Ribeiro da Costa, 2005; Marques et al., 2006). These samples record the pervasive serpentinization of Rainbow massif basement in a seawater-dominated context and are sulfide free (Debret et al., 2017). They will be referred to as non-mineralized serpentinites in the following sections. (2) The second group of samples displays mesh and bastite textures that have been partly to fully replaced by brownish serpentine during hydrothermal fluid circulation. This process is accompanied by precipitation of hydrothermal sulfides (mainly pyrite and pyrrhotite) and chloride minerals (Debret et al., 2017; Marques et al., 2007). These samples

will be referred to as mineralized serpentinites in the following sections. Although highly abundant within or near the stockwork area, they are not exclusively restricted to this area (Fig. 1; Appendix A).

3. Stable isotope analytical method

Major and trace elements analyses are from Ribeiro da Costa (2005), Marques et al. (2007) and Andreani et al. (2014) and are displayed in Appendices A and B. The Zn, Cu and Fe isotope measurements were carried out on the same whole-rock powders at the Laboratoire G-Time, Université Libre de Bruxelles (ULB). About 100 mg of powdered samples were dissolved using a 1:1 mix of concentrated HF and HCl in Parr bombs at 160 °C in an oven for 5 days. These were then further attacked with aqua regia, a 1:3 mix of concentrated HNO₃ and HCl for 3 days at 130 °C. Finally, samples were brought into solution in 6 M HCl prior to column chemistry. The whole procedure ensures full dissolution of refractory phases such as spinels. Quantitative purification of Zn, Cu and Fe was achieved by chromatographic exchange, using 1 ml of AG1-x8 (200–400 mesh) and 0.4 × 7 cm Teflon columns, following

the procedure developed by Sossi et al. (2015). All reagents used in the chemistry and mass spectrometry procedures were distilled and subboiled using Teflon two-bottle stills at the ULB. The total procedural blank contribution was <14 ng for Zn, <4 ng for Cu and <80 ng of Fe, which is negligible compared to the amount of Zn, Cu and Fe in the samples (blank contribution is <<1%).

3.1. Zn and Cu isotope analyses

Bulk rock Zn and Cu isotope data were obtained at the ULB (Laboratoire G-Time) on a Nu Plasma II Multi-Collector-Inductively Coupled Plasma-Mass Spectrometer (MC-ICP-MS Nu Instruments, Ltd.; for more details see Petit et al., 2008). The analyses were performed in wet plasma mode. Instrumental mass bias was corrected by sample-standard bracketing and external normalization (Cu- and Zn-doping technique for Zn and Cu measurements, respectively). Each sample was bracketed by two analyses of a standard (either Zn in-house JMC standard or Cu NIST SRM 976). Both sample and standard solutions were run at 400 ppb in 0.05M HNO₃, giving the same total beam intensity of 6 V. In addition to Zn and Cu masses, we also monitored ⁶²Ni to avoid interference between ⁶⁴Ni and ⁶⁴Zn. However, the ⁶²Ni beam intensity was systematically lower than the background signal, which indicates a complete Ni separation from the analysed solutions.

The $\delta^{66}\text{Zn}$ isotope composition of the samples is presented as a delta value in permil notation relative to the JMC-Lyon isotopic standard. $\delta^{68}\text{Zn}$ are also given to demonstrate mass dependency of the measurements. All reported errors are 2 standard deviations (2sd).

$$\delta^{66}\text{Zn} = \left(\left(\frac{{}^{66}\text{Zn}/{}^{64}\text{Zn}_{\text{sample}}}{{}^{66}\text{Zn}/{}^{64}\text{Zn}_{\text{JMC-Lyon}}} \right) - 1 \right) \times 10^3$$

$$\delta^{68}\text{Zn} = \left(\left(\frac{{}^{68}\text{Zn}/{}^{64}\text{Zn}_{\text{sample}}}{{}^{68}\text{Zn}/{}^{64}\text{Zn}_{\text{JMC-Lyon}}} \right) - 1 \right) \times 10^3$$

Due to a limited supply of the JMC-Lyon standard solution, samples were measured relative to an in-house standard. This standard is offset from JMC-Lyon by +0.09 (± 0.03 , 2sd)%₀ for $\delta^{66}\text{Zn}$ and by +0.18 (± 0.06)%₀ for $\delta^{68}\text{Zn}$ (over two years of measurements – $n \sim 200$); as such we were able to correct our measured value by this factor and present our data relative to JMC-Lyon, as widely accepted. During data acquisition, IRMM-3702 was analysed throughout each Zn session giving a mean $\delta^{66}\text{Zn}$ value of 0.30 ± 0.04 (2sd)%₀ and a mean $\delta^{68}\text{Zn}$ value of 0.61 ± 0.08 %₀, where n is 20, in excellent agreement with previously published measurements of this standard (Petit et al., 2008).

The $\delta^{65}\text{Cu}$ isotope composition of the samples is presented as a delta value in permil notation relative to the NIST SRM 976 Cu isotopic standard:

$$\delta^{65}\text{Cu} = \left(\left(\frac{{}^{65}\text{Cu}/{}^{63}\text{Cu}_{\text{sample}}}{{}^{65}\text{Cu}/{}^{63}\text{Cu}_{\text{NIST976}}} \right) - 1 \right) \times 10^3$$

Repeated measurements of the in-house NIST SRM 976 Cu gave an average $\delta^{65}\text{Cu}$ value of 0.00 ± 0.03 %₀ ($n = 9$). In addition to these, reference materials (BHVO2 basalt, UB-N and BCh6 serpentinites, LZ17a peridotite) were processed through columns and analysed for $\delta^{66}\text{Zn}$, $\delta^{68}\text{Zn}$ and $\delta^{65}\text{Cu}$ alongside samples. Data are displayed in Appendix B and are in good agreement with previous studies.

3.2. Fe isotope analyses

Bulk rock Fe isotope data were obtained at the ULB (Laboratoire G-Time) on a Nu Plasma II MC-ICP-MS in wet plasma and medium resolution mode. Instrumental mass bias was corrected by sample-standard bracketing. Both sample and standard solutions were run at 1 ppm in 0.05M HNO₃, giving the same total beam intensity of 13 V. Isotope ratios are reported as $\delta^{56}\text{Fe}$ in permil notation relative to IRMM-014 external standard, and $\delta^{57}\text{Fe}$ is

given to demonstrate mass dependency of the measurements. All reported errors are 2 standard deviations (2sd).

$$\delta^{56}\text{Fe} = \left(\left(\frac{{}^{56}\text{Fe}/{}^{54}\text{Fe}_{\text{sample}}}{{}^{56}\text{Fe}/{}^{54}\text{Fe}_{\text{IRMM-014}}} \right) - 1 \right) \times 10^3$$

$$\delta^{57}\text{Fe} = \left(\left(\frac{{}^{57}\text{Fe}/{}^{54}\text{Fe}_{\text{sample}}}{{}^{57}\text{Fe}/{}^{54}\text{Fe}_{\text{IRMM-014}}} \right) - 1 \right) \times 10^3$$

In addition to Fe masses, ⁵³Cr and ⁶⁰Ni were also monitored and online Cr and Ni corrections were applied to account for any isobaric interference from ⁵⁴Cr and ⁵⁸Ni on the ⁵⁴Fe and ⁵⁸Fe masses. These corrections were either negligible or non-existent due to the effective separation of Fe from Cr and Ni during column chemistry. An in-house standard MIX was analysed throughout each analytical sessions giving an average $\delta^{56}\text{Fe}$ value of $-1.55 (\pm 0.05, 2\text{sd})\%$ ₀ and average $\delta^{57}\text{Fe}$ value of $-2.30 (\pm 0.15, 2\text{sd})\%$ ₀, where $n = 12$. In addition, reference materials (BHVO2 basalt, UB-N and BCh6 serpentinites, LZ17a peridotite) were processed through columns and analysed alongside samples. The data are displayed in Appendix B and are in good agreement with previous studies.

4. Results

Zn, Cu and Fe concentrations and isotope ratios, together with Al₂O₃/SiO₂ and Fe³⁺/ΣFe ratios are given in Appendix B. The Rainbow serpentinized peridotites have refractory compositions, (e.g., dunite or pyroxene-poor harzburgites) characterized by low Al₂O₃/SiO₂ (<0.03) and high MgO/SiO₂ (>0.87) ratios (Fig. 2a). They display high loss on ignition (LOI) values (>12 wt%) and high Fe³⁺/ΣFe ratios (>0.4) compatible with high serpentinization degrees (Fig. 2b). Rainbow mineralized samples are characterized by the highest Fe³⁺/ΣFe values reported in abyssal or orogenic serpentinization settings (Fig. 2b).

As a whole, the Rainbow serpentinized peridotites display broad concentration ranges for Zn (25–1323 ppm), Cu (0.5–2168 ppm) and Fe₂O₃^{Total} (6.1–19.8 wt%). Metal concentrations increase from non-mineralized (Zn = 26–44 ppm; Cu = 1–13 ppm; Fe₂O₃ = 6.1–9.2 wt%) to mineralized (Zn = 53–1323 ppm; Cu = 0.5–2168 ppm; Fe₂O₃ = 6.5–19.8 wt%) samples. $\delta^{66}\text{Zn}$ and $\delta^{65}\text{Cu}$ data of Rainbow serpentinized peridotites vary from $-0.10 (\pm 0.03, 2\text{sd})$ to $+0.47 (\pm 0.01, 2\text{sd})\%$ ₀ and from $-0.93 (\pm 0.02, 2\text{sd})$ to $+0.24 (\pm 0.03, 2\text{sd})\%$ ₀, respectively. Those variations ($\sim 0.6\%$ ₀ for Zn isotopes and $\sim 1.1\%$ ₀ for Cu isotopes) are among the highest reported in an ultramafic massif, independent of the context (abyssal or orogenic; Fig. 3). The $\delta^{66}\text{Zn}$ values of Rainbow serpentinized peridotites progressively decrease from non-mineralized ($+0.30 \pm 0.07\%$ ₀ $\leq \delta^{66}\text{Zn} \leq +0.47 \pm 0.01\%$ ₀, 2sd), which display high $\delta^{66}\text{Zn}$ relative to primitive mantle (PM, $\delta^{66}\text{Zn}_{\text{PM}} = 0.16 \pm 0.06\%$ ₀, Sossi et al. (2018), to mineralized samples ($-0.10 \pm 0.03\%$ ₀ $\leq \delta^{66}\text{Zn} \leq +0.29 \pm 0.03\%$ ₀, 2sd). Given that serpentinized peridotites have relatively low Cu concentrations (<10 ppm), only one non-mineralized sample was analysed for Cu isotopes. This sample (M7-PL04-6) displays a $\delta^{65}\text{Cu}$ of $+0.24 \pm 0.03\%$ ₀, higher than the primitive mantle value ($\delta^{65}\text{Cu}_{\text{PM}} = +0.07 \pm 0.1\%$ ₀, Savage et al., 2015; Fig. 3) and close to the analysis reported by Rouxel et al. (2004; $\delta^{65}\text{Cu} = +0.14\%$ ₀). The mineralized samples ($-0.93 \pm 0.02\%$ ₀ $\leq \delta^{65}\text{Cu} \leq +0.24 \pm 0.03\%$ ₀, 2sd) display a large range of $\delta^{65}\text{Cu}$ values, most of them being relatively light compared to non-mineralized samples (Appendix B, Fig. 3). The $\delta^{56}\text{Fe}$ of non-mineralized samples vary from $-0.14 (\pm 0.08)$ to $+0.08 (\pm 0.01)\%$ ₀ and are close to those reported in other abyssal or orogenic contexts (Fig. 3). The mineralized samples display a large range of $\delta^{56}\text{Fe}$ ($-0.15 \pm 0.08\%$ ₀ $\leq \delta^{56}\text{Fe} \leq +0.25 \pm 0.06\%$ ₀) with samples from the Rainbow stockwork (IR-DR01-A-05 and FL-PL08-05; Fig. 1) displaying the heaviest values (Fig. 3).

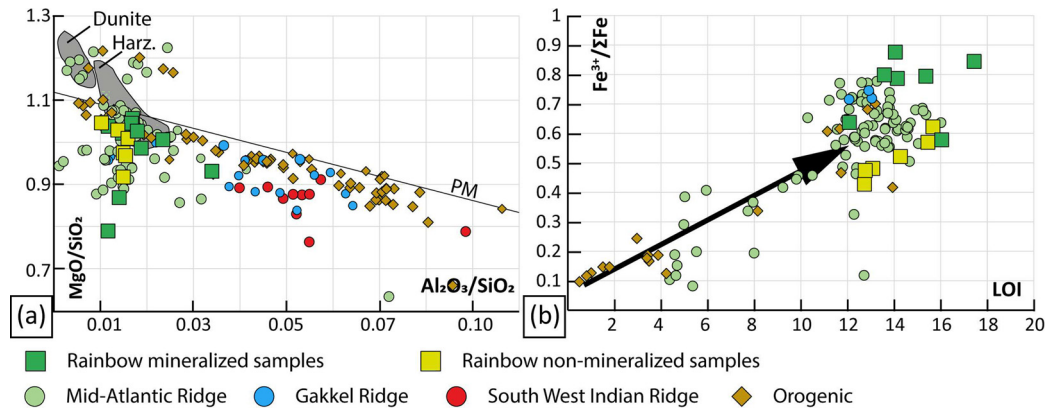


Fig. 2. Plots of (a) MgO/SiO_2 vs $\text{Al}_2\text{O}_3/\text{SiO}_2$ and (b) $\text{Fe}^{3+}/\Sigma\text{Fe}$ vs Loss On Ignition (LOI, in wt.%) in abyssal serpentinized peridotites. Because abyssal peridotites often display a high serpentinization degree, the characterization of peridotite fertility is better assessed by $\text{Al}_2\text{O}_3/\text{SiO}_2$ ratio rather than Al_2O_3 concentrations (Godard et al., 2008). The thin black line on Fig. 2a represents the primitive mantle (PM) ratios and the grey fields correspond to dunite and harzburgite compositions (after Godard et al., 2008). On Fig. 2a, changes in whole-rock ratios of both MgO/SiO_2 and $\text{Al}_2\text{O}_3/\text{SiO}_2$ accompany the transition (left to right) of depleted (e.g., dunite) to enriched (e.g., lherzolite) peridotites (grey fields are from Godard et al., 2008). On Fig. 2b, changes in whole-rock $\text{Fe}^{3+}/\Sigma\text{Fe}$ ratio and LOI accompany the transition (left to right) of fresh peridotite to fully serpentinized peridotite. The high LOI values (>12 wt.%) probably reflect a high amount of brucite, talc, sulfides, organic carbons, carbonates and/or clay minerals. Compilation of abyssal peridotite and orogenic peridotite compositions are from: Pindos (Bonnemains et al., 2016), Alps (Debret et al., 2013; Sossi et al., 2018), and Horoman (Takazawa et al., 2000) for orogenic contexts; IODP sites 1270 & 1271 (Paulick et al., 2006) and ODP Leg 153 (MARK region; Andreani et al., 2014; Bonnemains et al., 2016) for Mid-Atlantic Ridge; Vancouver Leg 7 (Craddock et al., 2013) for the South West Indian Ridge (SWIR); western half of the Gakkel ridge from 5°W to 85°E , with peridotites recovered primarily between 3 and 29°E in the Sparsely Magmatic Zone (Craddock et al., 2013; this study) for Gakkel ridge.

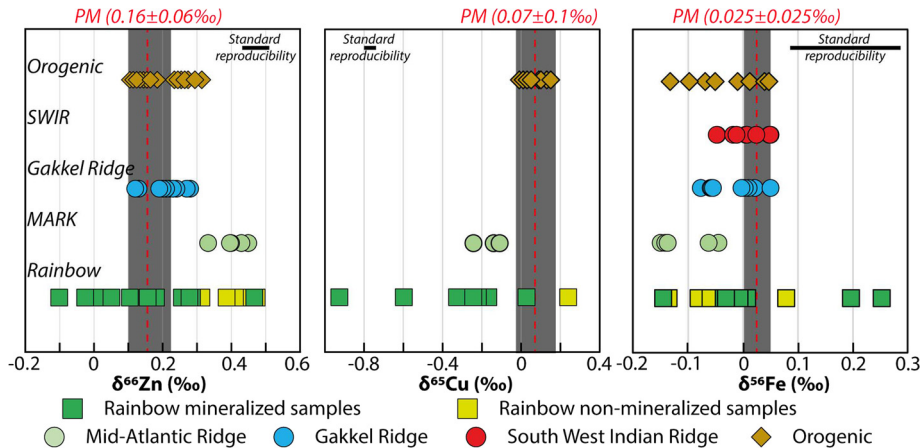


Fig. 3. Zn, Cu and Fe isotopic ranges of orogenic and abyssal peridotites. The grey boxes and red dotted lines show the composition of the Primitive Mantle (PM) after Sossi et al. (2018), Savage et al. (2015) and Craddock et al. (2013) for $\delta^{66}\text{Zn}$, $\delta^{65}\text{Cu}$ and $\delta^{56}\text{Fe}$, respectively. The isotope compositions are reported for orogenic serpentinized peridotites (Ben Othman et al., 2006; Ikehata and Hirata, 2012; Debret et al., 2016 – SSP: Slightly Serpentinized Peridotites and Liz-serpentinites; Pons et al., 2016 – SSP and Liz-serpentinites – and Sossi et al., 2018 – Balmuccia), Gakkel Ridge serpentinized peridotites (Pons et al., 2011; Craddock et al., 2013 – unweathered samples), MARK and Rainbow (this study). (For interpretation of the colours in the figure(s), the reader is referred to the web version of this article.)

5. Discussion

The Rainbow serpentinized peridotites display a large range of Zn, Cu or Fe concentrations and isotopic values, overlapping the whole range of terrestrial ultramafic rock compositions (Figs. 3 and 4). This variability reflects a high mobility of metals during Rainbow massif formation which can be induced by: (1) mantle heterogeneities and/or melt/rock interactions occurring below the massif and prior to serpentinization, (2) serpentinization of the ultramafic basement at relatively low temperature ($<250^\circ\text{C}$) and/or (3) mineralization of serpentinized peridotites at high temperature ($>350^\circ\text{C}$) during hydrothermal fluid circulation below the Rainbow stockwork. The influence of kinetic effects, related to the preferential mobility of isotopically light species during fluid/rock interactions or diffusion processes, can be ruled out as the direction of diffusive transport from solid (Zn-, Cu- and Fe-rich) to fluid (Zn-, Cu- and Fe-poor) would result in heavy $\delta^{66}\text{Zn}$, $\delta^{65}\text{Cu}$ and $\delta^{56}\text{Fe}$ in the residue and therefore generate covariations between $\delta^{66}\text{Zn}$, $\delta^{65}\text{Cu}$ and $\delta^{56}\text{Fe}$ in the studied samples (e.g., Pogge von Strandmann et al., 2015), which are not observed. In the fol-

lowing sections we discuss the impact of these three processes on metal concentrations and stable isotope variations in abyssal serpentinized peridotites.

5.1. Mantle heterogeneities

Zn elemental and isotopic compositions in peridotites are primarily controlled by their fertility (Doucet et al., 2016; Moynier et al., 2017), with fertile peridotites (e.g., high $\text{Al}_2\text{O}_3/\text{SiO}_2$; Fig. 4) displaying high Zn concentrations and relatively heavy $\delta^{66}\text{Zn}$ (e.g., $\delta^{66}\text{Zn}_{\text{pyroxenite}} \sim +0.20 \pm 0.02\text{‰}$ and up to 70 ppm of Zn; Sossi et al., 2018) and refractory peridotites displaying relatively low Zn concentrations and light $\delta^{66}\text{Zn}$ (e.g., $\delta^{66}\text{Zn}_{\text{dunite}} \sim +0.14 \pm 0.02\text{‰}$ and down to 41 ppm of Zn; Sossi et al., 2018). The Rainbow non-mineralized samples have low Zn concentrations (26–44 ppm) and high $\delta^{66}\text{Zn}$ ($+0.30\text{‰} < \delta^{66}\text{Zn} < +0.47\text{‰}$) relative to dunite while the mineralized samples display a large range of Zn concentrations (47–1323 ppm) and $\delta^{66}\text{Zn}$ ($-10\text{‰} < \delta^{66}\text{Zn} < +0.26\text{‰}$). These values are incompatible with the refractory composition of Rainbow samples (Fig. 2a). In addition, no correlation between Zn concen-

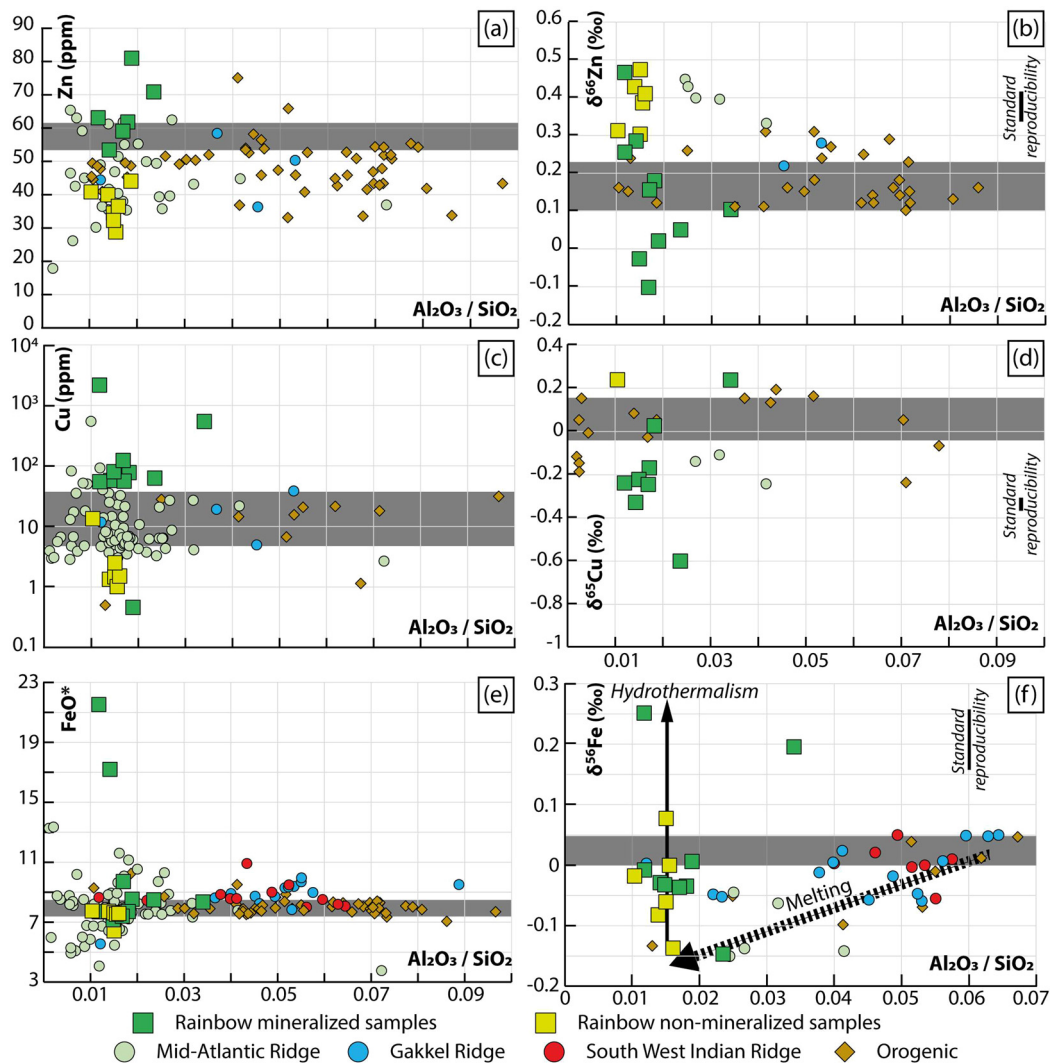


Fig. 4. Plots of Zn, Cu, FeO concentrations and $\delta^{66}\text{Zn}$, $\delta^{65}\text{Cu}$, $\delta^{56}\text{Fe}$ of abyssal and orogenic ultramafic rocks vs a mantle fertility proxy ($\text{Al}_2\text{O}_3/\text{SiO}_2$). The grey lines correspond to primitive mantle variations for Zn, Cu and FeO (Jagoutz et al., 1979; McDonough and Sun, 1995) and for $\delta^{66}\text{Zn}$ (Sossi et al., 2018) and $\delta^{65}\text{Cu}$ (Savage et al., 2015). In Fig. 4f, the grey field corresponds to upper mantle compositional variations (Debret et al., 2016). The isotope compositions of orogenic samples are from Ben Othman et al. (2006), Ikehata and Hirata (2012), Debret et al. (2016 – SSP and Liz-serpentinites), Pons et al. (2016 – SSP and Liz-serpentinites) and Sossi et al. (2018 – Balmuccia), Gakkell Ridge from Pons et al. (2011), Craddock et al. (2013 – unweathered samples) and Debret et al. (2016), SWIR (South West Indian Ridge) from Craddock et al. (2013 – unweathered samples), Mid-Atlantic Ridge and Rainbow from this study. *Composition recalculated in wt.% on a volatile free basis.

trations or $\delta^{66}\text{Zn}$ and peridotite fertility (e.g., $\text{Al}_2\text{O}_3/\text{SiO}_2$) have been observed (Fig. 4a, b). This shows that abyssal peridotites do not preserve their initial Zn concentrations or $\delta^{66}\text{Zn}$ values during serpentinization at mid-oceanic ridges.

In the Rainbow massif, non-mineralized samples display homogeneous and low Cu concentrations (1–13 ppm) relative to primitive mantle. However, there are no systematic changes of Cu concentrations or isotope values with peridotite fertility (e.g., $\text{Al}_2\text{O}_3/\text{SiO}_2$; Fig. 4c, d). This suggests that partial melting has only a limited effect on Cu concentrations or $\delta^{65}\text{Cu}$ of abyssal peridotites. In good agreement with this, only limited $\delta^{56}\text{Cu}$ variations have been observed in fresh peridotites from orogenic massifs ($\delta^{65}\text{Cu} = +0.07 \pm 0.09\%$, Ikehata and Hirata, 2012; Othman et al., 2006), while the $\delta^{65}\text{Cu}$ values of magmatic differentiation sequences ($-0.08\% < \delta^{65}\text{Cu} < +0.20\%$; Savage et al., 2015) largely overlap with those of primitive mantle ($\delta^{65}\text{Cu}_{\text{PM}} = +0.07 \pm 0.10\%$; Savage et al., 2015; Fig. 4d). Therefore, the variations of Cu concentrations and $\delta^{65}\text{Cu}$ (Fig. 4c, d) observed in Rainbow serpentinized peridotites cannot be explained by melt/rock interaction processes occurring prior the serpentinization process.

Fe concentrations in abyssal peridotites and serpentinites are relatively constant, with the exception of few mineralized samples that display abnormally high FeO concentrations (Fig. 4e). This reflects a low mobility of Fe in fluids relative to initial peridotite Fe concentrations. Several studies have shown that the $\delta^{56}\text{Fe}$ of peridotites are influenced by partial melting, with lherzolites or clinopyroxenites displaying high $\delta^{56}\text{Fe}$ relative to dunites (Debret et al., 2016; Williams et al., 2005). In the Rainbow massif, non-mineralized samples have $\delta^{56}\text{Fe}$ ranging from $-0.14 \pm 0.03\%$ to $+0.08 \pm 0.01\%$ with an average value of $-0.04 \pm 0.02\%$. These values are lower than those reported for Gakkell Ridge and South West Indian Ridge serpentinized peridotites, which display average values of $+0.01 \pm 0.01\%$ and $+0.02 \pm 0.01\%$, respectively (Craddock et al., 2013). As illustrated in Fig. 4f, the $\delta^{56}\text{Fe}$ of abyssal and orogenic peridotites and serpentinites form a broad positive array with $\text{Al}_2\text{O}_3/\text{SiO}_2$, with depleted peridotites ($\text{Al}_2\text{O}_3/\text{SiO}_2 < 0.04$) having $\delta^{56}\text{Fe}$ inferior to that of primitive mantle and fertile peridotites ($\text{Al}_2\text{O}_3/\text{SiO}_2 > 0.04$) having $\delta^{56}\text{Fe}$ close to that of primitive mantle ($+0.025 \pm 0.025\%$; Craddock et al., 2013). This provides evidence for some level of source fertility control on protolith $\delta^{56}\text{Fe}$ of Rainbow serpentinized peridotites. In that sense, the rel-

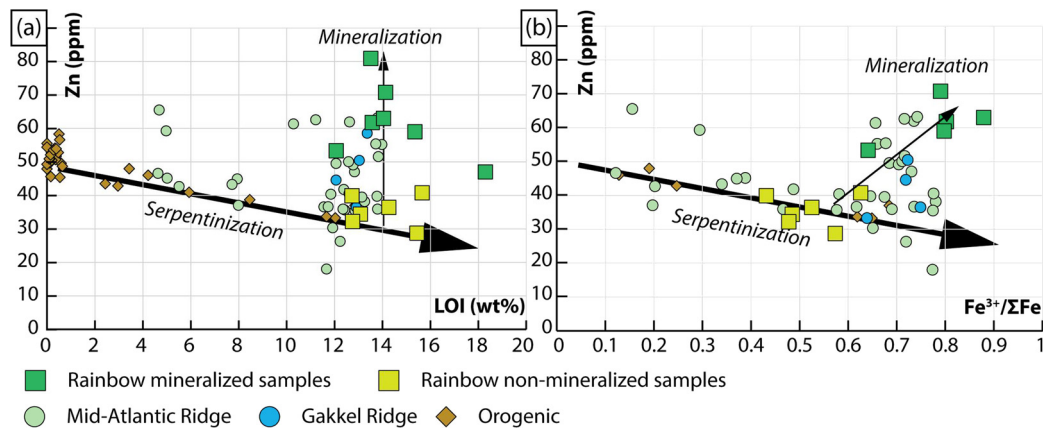


Fig. 5. Zn concentrations in ppm vs proxies of the serpentinization process (LOI in wt% and $\text{Fe}^{3+}/\Sigma\text{Fe}$). Zn concentrations of peridotites progressively decrease during the serpentinization process. Mineralized samples are comparatively enriched in Zn.

atively low $\delta^{56}\text{Fe}$ average value of non-mineralized samples ($\delta^{56}\text{Fe} = -0.04 \pm 0.02\text{‰}$) can be attributed to their refractory composition. It should however be noted that few Rainbow samples are offset to higher $\delta^{56}\text{Fe}$ values, with some mineralized samples displaying values as high as $+0.25\text{‰}$ (Fig. 4f), implying mobility of Fe near the Rainbow stockwork.

5.2. Serpentinization of the Rainbow massif basement (non-mineralized samples)

Zinc and copper concentrations in Rainbow non-mineralized samples are low relative to those of primitive mantle (Fig. 4a, c). In addition, Zn concentrations correlate positively with serpentinization indices (e.g., LOI or $\text{Fe}^{3+}/\Sigma\text{Fe}$ ratio; Fig. 5), suggesting that these elements are leached by fluids during serpentine formation. In agreement with this scenario, a positive correlation between $\delta^{66}\text{Zn}$ and serpentinization indices exists among non-mineralized samples (Fig. 6a). This provides evidence for a preferential mobility of isotopically light Zn in fluids during the serpentinization process. It should be noted that, although the $\delta^{65}\text{Cu}$ of non-mineralized samples are close to that of the primitive mantle (Fig. 3), we do not rule out that serpentinization may fractionate Cu isotopes as only few samples have been analysed in this or in previous studies (e.g., Rouxel et al., 2004). The $\delta^{56}\text{Fe}$ values of non-mineralized samples overlap that of primitive mantle and no correlation between $\delta^{56}\text{Fe}$ and serpentinization indices has been observed. This suggests that Fe isotopes remain unfractionated in bulk rock during the serpentinization process, and thus this element is poorly mobile and/or fractionated in seawater relative to the initial composition of the peridotite (see also Craddock et al., 2013; Debret et al., 2016 for similar conclusions in abyssal and orogenic contexts).

Therefore, Zn elemental and isotopic compositions are the most sensitive tracers of serpentinization effects in abyssal peridotites. Zn concentrations in serpentinized peridotites are highly sensitive to sulfide and spinel crystallization and/or dissolution, as both minerals can display high Zn concentrations (up to several hundreds of ppm; e.g., Guo et al., 1999; Wang et al., 2017) relative to mantle silicates (about 10–50 ppm) or serpentines (10–40 ppm, e.g., Debret et al., 2013; Rouméjon et al., 2015). Serpentinization of abyssal peridotites is accompanied by progressive disappearance of mantle minerals including the oxidation of mantle sulfides into sulfate-bearing serpentine (Debret et al., 2017) and the recrystallization of mantle spinels into magnetite, Cr-spinel and ferrichromite (e.g., Marques et al., 2007). Leaching of Zn during serpentinization can therefore be a direct consequence of mantle sulfide and spinel dissolution during the serpentinization process.

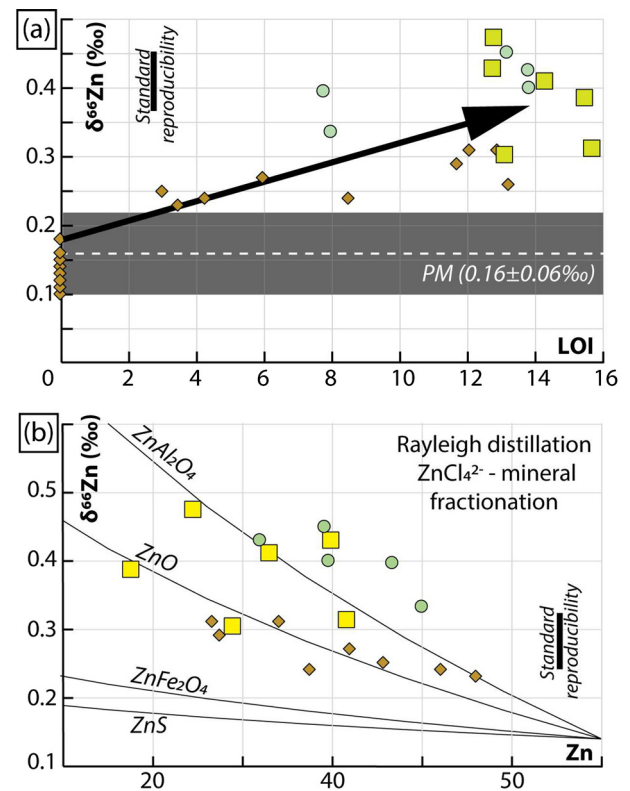


Fig. 6. (a) Plot of $\delta^{66}\text{Zn}$ (‰) vs LOI (wt%). During the serpentinization of abyssal peridotite, the progressive increase of the LOI is correlated with an increase of $\delta^{66}\text{Zn}$. (b) Distribution of $\delta^{66}\text{Zn}$ (‰) and Zn (ppm) concentrations in abyssal and orogenic serpentinized peridotites (samples with a LOI superior to 0 wt%). Abyssal peridotites/serpentinites display relatively high $\delta^{66}\text{Zn}$ and low Zn concentrations relative to primitive mantle. The distribution of $\delta^{66}\text{Zn}$ (‰) and Zn (ppm) concentrations is modelled by the leaching of ZnCl_4^{2-} anions during dissolution of sulfide (ZnS) and spinels (ZnAl_2O_4 , ZnO, ZnFe_2O_4 ; black lines – see text for more details). The starting composition is a dunite in agreement with the refractory composition of Rainbow samples. It should be noted that MARK samples display high $\delta^{66}\text{Zn}$ and Zn concentrations relative to Rainbow samples. This can be attributed to their relatively fertile composition.

Previous studies have shown that sulfur and carbon are largely retained during serpentinization (e.g., Alt and Shanks, 2003; Debret et al., 2017; Delacour et al., 2008), while chlorine is abundant in fluids in abyssal context. In addition, Zn complexation with sulfate or carbon in fluids will lead to the preferential mobility of heavy Zn (e.g., Pons et al., 2016) and therefore cannot be invoked to explain the increase of $\delta^{66}\text{Zn}$ in abyssal peridotites during ser-

pentinization. We therefore attempt to model the leaching of Zn during the dissolution of sulfides and spinel in abyssal peridotites by chlorine-bearing fluids (ZnCl_4^{2-}). In these models, the elemental and isotopic behaviour of Zn in whole rock is approximated to that of sulfide or spinels (i.e., β -factor). We used the *ab initio* calculations of Fujii et al. (2014) for $[\text{ZnCl}_4^{2-}]$ complex in fluids and those of Ducher et al. (2016) for sphalerite (ZnS) and for different spinel endmembers, namely franklinite (ZnFe_2O_4), gahnite (ZnAl_2O_4) and zincite (ZnO). It should be noted that, to our knowledge, no equilibrium zinc isotope fractionation factors in Zn-bearing chromite are available yet in the literature. The $\delta^{66}\text{Zn}$ evolution of abyssal peridotite during serpentinization was then modelled using a simple Rayleigh distillation model, according to the following equations:

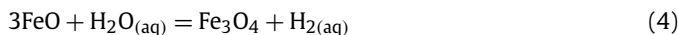
$$10^3 \ln(\alpha_{\text{fluid-mineral}}) = 10^3 \ln(\beta_{\text{fluid}}) - 10^3 \ln(\beta_{\text{mineral}})$$

$$\delta^{66}\text{Zn}_{\text{Final}} = (1000 + \delta^{66}\text{Zn}_{\text{Initial}}) \times (F^{(\alpha-1)} - 1) + \delta^{66}\text{Zn}_{\text{Initial}}$$

where α is the fractionation factor between sulfides or spinels and a fluid phase complexing Zn as $[\text{ZnCl}_4^{2-}]$ at 200 °C; F is the fraction of Zn remaining in the rock, ranging from 1 (unreacted) to 0 (all of Zn lost to the fluid phase), $\delta^{66}\text{Zn}_{\text{Initial}}$ was set to a dunite-like value (0.14‰; e.g., Sossi et al., 2018). Results of these models are displayed in Fig. 6b. Surprisingly, the dissolution of sulfide has only a limited effect on $\delta^{66}\text{Zn}$ of abyssal peridotites. At the opposite, the progressive disappearance of mantle spinels during serpentinization can lead to strong isotopic fractionation, up to ~1‰. Both processes, sulfide and spinel dissolutions, can lead to a decrease of Zn concentrations and/or an increase of $\delta^{66}\text{Zn}$ therefore explaining the whole set of compositions of non-mineralized abyssal or orogenic serpentinized peridotites (Fig. 6b).

5.3. Hydrothermal fluid circulation and serpentinite mineralization

Hydrothermal circulation near and within the Rainbow stockwork leads to sulfide crystallization (Marques et al., 2006; Fouquet et al., 2010; Debret et al., 2017) and to an increase of chalcophile element concentration (e.g., As, Sb, Zn, Cu) in serpentinized peridotites, showing that both Zn and Cu are transported by sulfur-bearing fluids (Marques et al., 2007; Andreani et al., 2014; Debret et al., 2017). Mineralized samples display high $\text{Fe}^{3+}/\Sigma\text{Fe}$ ratios (0.58–0.88) relative to non-mineralized serpentinites (0.43–0.63; Figs. 2 and 5), suggesting that the mineralization process is associated with Fe oxidation. However, if magnetite is the main Fe^{3+} -carrier in the sampled serpentinites, the $\text{Fe}^{3+}/\Sigma\text{Fe}$ values are too high to be only controlled by magnetite precipitation ($\text{Fe}^{3+}/\Sigma\text{Fe} \sim 0.67$), suggesting crystallization of Fe^{3+} -bearing serpentine (e.g., Andreani et al., 2013). Abundant magnetite precipitation associated with localized hydrothermal circulation is in good agreement with the existence of strong magnetic anomalies localized right below the Rainbow hydrothermal field (Szitkar et al., 2014). Similar features have been observed in ophiolites where abundant magnetite precipitation has been enhanced by hydrothermal fluid circulation during the opening of the Alpine Tethys (Toffolo et al., 2017). This process is likely to be favoured by the circulation of high temperature fluids (Klein et al., 2014) and certainly contributes to the release of high amounts of H_2 (Eq. (4)) at vents (Charlou et al., 2002):



However, this strong and localized Fe enrichment and oxidation at depth cannot be related to serpentinization alone, which classically produces a lower “background” magnetic signal (i.e. the one

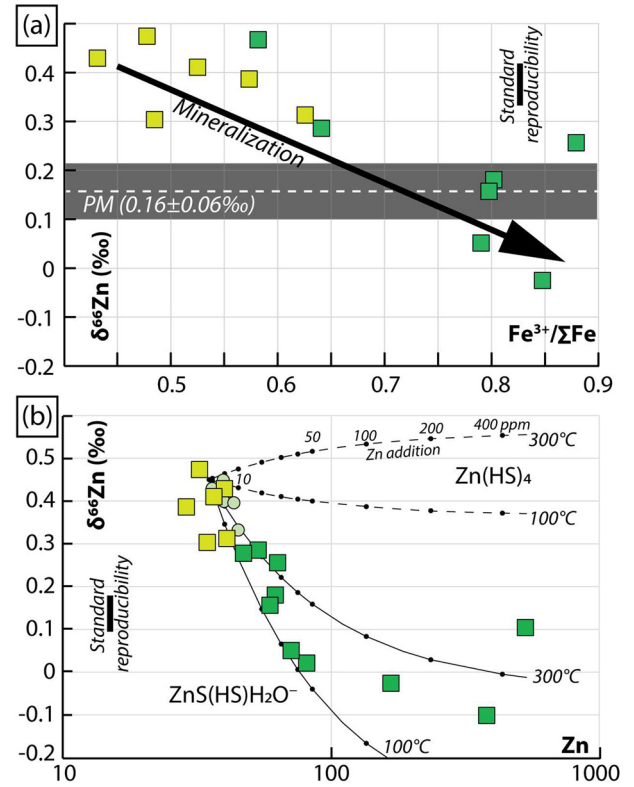


Fig. 7. (a) Plot of $\delta^{66}\text{Zn}$ (‰) versus $\text{Fe}^{3+}/\Sigma\text{Fe}$ in Rainbow ultramafic samples. The mineralization of the serpentinized peridotites is accompanied with a decrease of both $\delta^{66}\text{Zn}$ and $\text{Fe}^{3+}/\Sigma\text{Fe}$ values. (b) Plot of $\delta^{66}\text{Zn}$ (‰) versus Zn concentrations in Rainbow ultramafic samples. The decrease of $\delta^{66}\text{Zn}$ is accompanied by a gain in Zn. The black lines correspond to mixing model results: addition of Zn by $\text{ZnS}(\text{HS})\text{H}_2\text{O}$ or $\text{Zn}(\text{HS})_4$ fluids at temperatures of 100 and 300 °C.

of the surrounding rocks; e.g., Bonnemains et al., 2016), or high temperature conditions alone since high temperature hydrothermal areas are not always associated with magnetic anomalies (Szitkar et al., 2014), thus calling for an alternative reaction pathway and Fe source.

The increase of $\text{Fe}^{3+}/\Sigma\text{Fe}$ ratios in mineralized samples is associated with an increase of Zn and Cu concentrations and a decrease of $\delta^{66}\text{Zn}$ and $\delta^{65}\text{Cu}$ values (Appendix B, Fig. 7). This suggests addition of light Zn and Cu by fluids during ultramafic rock mineralization within and near the stockwork (Fig. 8a). Geologic evidences of gabbros intruding peridotites at depth are common in the Rainbow massif, corroborated by geophysically-imaged magma lenses at depth (e.g., Andreani et al., 2014; Canales et al., 2017; Dunn et al., 2017; Marques et al., 2006, 2007). These melts can thus provide a heat source for hydrothermal circulation at depth (Fig. 8a), after a phase of low-temperature serpentinization, that may have occurred at the periphery of the stockwork (Fig. 8a) and/or during exhumation and therefore while the Rainbow detachment was active (Fig. 8b). In addition, the reaction between seawater and gabbro at relatively high temperature (>350 °C) can leach magmatic sulfide and produce HS-bearing fluids with low pH (Alt and Shanks, 2003), comparable to Rainbow hydrothermal fluids, providing a potential source for light Zn and Cu in fluids (Fig. 8a). To further explore this link, we modelled sulfide mineralization in Rainbow serpentinized peridotites by gabbro-derived fluids in the following section.

There are at this time almost no constraints on Zn speciation in hydrothermal fluids at mid-oceanic ridges. We first attempted to model hydrothermal fluid isotopic composition during sulfide dissolution in gabbros by using a Rayleigh model and a large range of fluid compositions, for which *ab initio* calculations are

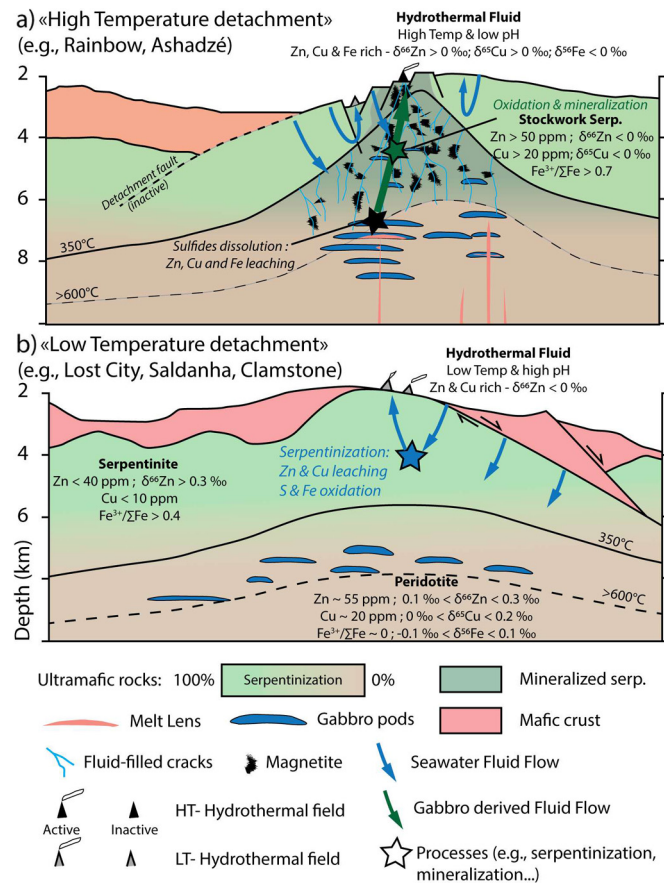


Fig. 8. Conceptual model illustrating reaction pathways beneath hydrothermal fields. Core complex internal structures are based on seismic reflection images from Canales et al. (2017). (a) The emplacement of hot and ductile gabbros at depth provides heat and leads to a high temperature hydrothermal circulation. The leaching of magmatic sulfides at depth enhances the formation of sulfur bearing fluids and the preferential mobility of Zn, Cu and Fe in fluids. The oxidation of these fluids below the stockwork enhance serpentine mineralization and the formation of hydrothermal deposits with heavy Zn, Cu and light Fe signatures. (b) Seawater percolates at depth through fractures in the footwall of detachment faults and enhanced the serpentinization of mantle peridotites. This episode is accompanied by the leaching of Cu and Zn by seawater derived fluids, which preferentially transport isotopically light Zn. The release of fluids can potentially enhance the formation of low temperature and low pH white smokers and the precipitation of Zn- and Cu-bearing hydrothermal deposits with low $\delta^{66}\text{Zn}$.

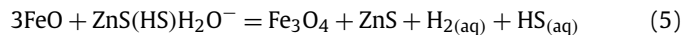
available ($\text{Zn}(\text{HS})_2(\text{H}_2\text{O})_4$; $\text{Zn}(\text{HS})_4$; $\text{ZnS}(\text{HS})\text{H}_2\text{O}^-$; $\text{ZnSO}_4(\text{H}_2\text{O})_6$; $\text{Zn}(\text{H}_2\text{O})_6^{2+}$; ZnCl_4^{2-} ; $\text{ZnCl}_3(\text{H}_2\text{O})^-$), and temperatures (from 100 to 300 °C; Appendix C). The dissolution of sphalerite during Zn leaching by fluids was fixed to an advanced stage ($F = 0.1$) and modelled using the *ab initio* calculation of Fujii et al. (2014), the compilation is from Moynier et al., (2017) and Ducher et al. (2016). The initial $\delta^{66}\text{Zn}$ of sphalerite was taken from Maréchal et al. (1999). The composition of Rainbow mineralized samples was then considered to be a binary mixture between non-mineralized samples and gabbro-derived fluids:

$$\delta^{66}\text{Zn}_{\text{mixture}} = (N_a\delta^{66}\text{Zn}_a + N_b\delta^{66}\text{Zn}_b) / (N_a + N_b)$$

where N_a and N_b are the amounts of Zn transported by fluids and the initial abundance of Zn in a non-mineralized serpentine, respectively. The whole data set of Rainbow mineralized samples can be explained by the percolation of $\text{Zn}(\text{HS})_2(\text{H}_2\text{O})_4$ or $\text{ZnS}(\text{HS})\text{H}_2\text{O}^-$ fluids at temperatures ranging from 100 °C to 300 °C (Fig. 7 and Appendix C). At the opposite, percolation of either $\text{Zn}(\text{HS})_4$ or ZnCl_4^{2-} fluids will drive serpentinized peridotites toward heavier values, while the percolation of $\text{ZnSO}_4(\text{H}_2\text{O})_6$,

$\text{Zn}(\text{H}_2\text{O})_6^{2+}$ or $\text{ZnCl}_3(\text{H}_2\text{O})^-$ fluids will produce serpentinized peridotites with lighter values (Fig. 7 and Appendix C). It should be noted that the mineralized sample FL-08-05 (Appendix B) displays high $\delta^{66}\text{Zn}$ and Zn concentrations, compatible with the existence of $\text{Zn}(\text{HS})_4$ fluids in the stockwork. This suggests that the formation of $\text{Zn}(\text{HS})_2(\text{H}_2\text{O})_4$ or $\text{ZnS}(\text{HS})\text{H}_2\text{O}^-$ complexes could occur through mixing between seawater (H_2O -rich) and fluids interacting with gabbros at depth (HS-rich).

The striking correspondence between the model predictions and our Zn isotope and concentration measurements provides strong evidence that $\text{Zn}(\text{HS})_2(\text{H}_2\text{O})_4$ and $\text{ZnS}(\text{HS})\text{H}_2\text{O}^-$ (Fig. 7) are the main Zn complexes in the fluid during the mineralization of serpentinites. Such fluids have the potential to enhance further Fe oxidation of Fe and sulfide precipitation in serpentinites, as well as the production of H_2 at the Rainbow field, e.g.:



The source of Fe during this reaction is assumed to be hosted by the rock. However, recent studies have underlined that Fe can be mobile in S-bearing fluids (Debret et al., 2016) and the measured Fe contents in Rainbow fluids are among the highest reported on MAR (~24000 mM; Charlou et al., 2002) suggesting that a certain amount of Fe is transported from the gabbros to the serpentinized peridotites by fluids. In good agreement with this, Rainbow mineralized samples can display abnormally high amounts of S (>1 wt%; Marques et al., 2006, 2007), Fe (up to 19.8 wt% of Fe_2O_3) and high $\delta^{56}\text{Fe}$ values (up to 0.25 ‰) relative to mantle peridotite field (Figs. 3, 4c, f). It should be noted that no correlation between Fe concentrations and $\delta^{56}\text{Fe}$ is observed in mineralized samples. This can be attributed to variability in $\delta^{56}\text{Fe}$ compositions either in the serpentine protolith (e.g., from -0.15 ‰ to +0.10 ‰, Fig. 3) and/or in fluids circulating at depth, whose composition is likely to evolve during the emplacement of magmatic pods at depth, the tectonic evolution of the massif and over time (e.g., Severmann et al., 2004). As Fe is considered to be mobile as Fe(II) and immobile as Fe(III), this suggests that the local oxidation of Fe near the surface may lead to the concomitant precipitation of sulfide and magnetite in serpentinites. Previous natural and theoretical studies have also demonstrated that magnetite and pyrite precipitating in equilibrium hydrothermal conditions should be enriched in heavy Fe isotopes (Blanchard et al., 2009; Scott et al., 2017; Syverson et al., 2014) explaining the heavy values of serpentinites nearby the Rainbow stockwork. Hence, the co-precipitation of magnetite and pyrite below the stockwork can result in the preferential partitioning of isotopically light Fe and heavy Zn and Cu in hydrothermal fluids (Fig. 8a). This observation is in agreement with previous Fe and Cu isotope studies that report hydrothermal deposits and/or fluids with light Fe and heavy Cu isotopic signature near vent chimneys in high temperature systems (e.g., Lucky Strike, Rainbow; Beard et al., 2003; Rouxel et al., 2004, 2008; Severmann et al., 2004).

6. Conclusions

Rainbow serpentinized peridotites display highly variable metal concentrations and transition-metal isotopic values, among the highest reported in abyssal or orogenic settings. These variations result from a two-stage process (Fig. 8) first enhanced (1) at low temperature by the leaching of Zn and Cu during pervasive serpentinization of ultramafic basement, in a seawater-dominated system and (2) by addition of Zn, Cu and Fe during the localized circulation of high temperature (>350 °C) gabbro-derived fluids near the Rainbow stockwork.

During serpentinization of abyssal peridotites in seawater-dominated systems, Zn and Cu are progressively leached by fluids

(Fig. 8b). This process is accompanied by an increase of bulk-rock $\delta^{66}\text{Zn}$ values, suggesting the preferential leaching of isotopically light Zn by fluids. Geochemical models show that the fractionation of Zn isotopes during serpentinization is controlled by the dissolution of both mantle sulfide and/or spinels and Zn complexation with chlorine in fluids. At the opposite, Fe isotopic variations in abyssal serpentinites are inherited from peridotite protoliths suggesting that this element is poorly mobile in seawater-dominated systems (i.e., no interactions between seawater and gabbros prior to the serpentinization process). This reaction pathway is likely to occur in various low temperature abyssal environments, near the surface during the pervasive serpentinization of mantle peridotites (serpentinization gradient affecting the first kilometres of the lithosphere; Fig. 8b) and/or away from major heating sources (e.g., magmatic intrusions; Fig. 8a). It can lead to the precipitation of Zn- and Cu-ore deposits with light $\delta^{66}\text{Zn}$ signatures near low temperature vent chimneys in ultramafic systems (e.g., Lost City, Saldanha or Clamstone).

Localized high temperature hydrothermal circulation at the summit of Rainbow massif enhanced the mineralization of serpentinites. This process is associated with significant sulfide and magnetite precipitation and leads to an increase of $\text{Fe}^{3+}/\Sigma\text{Fe}$, FeO^{Tot} , Zn and Cu concentrations in serpentinites, as well as isotopic fractionation of Zn, Cu and Fe. This suggests high metal mobility in Rainbow hydrothermal fluids. Indeed, geochemical models show that leaching of magmatic sulfides at depth enhance metal mobility and the transport of Zn, Cu and Fe by sulfur complexes in fluids. The oxidation of these fluids during their migration toward the surface leads to mineralization and isotopic fractionation of Zn, Cu and Fe in serpentinized peridotites. This process is associated with a production of H_2 and can lead to the precipitation of ore deposits with heavy $\delta^{66}\text{Zn}$ and $\delta^{65}\text{Cu}$ and light $\delta^{56}\text{Fe}$ near the venting area of high temperature systems (e.g., Rainbow, Ashadzé).

The study of the Rainbow ultramafic basement and stockwork shows that serpentinization can generate fluids with distinct compositions and isotopic signatures, depending on the fluid temperature, geological setting (tectonic vs magma-dominated) and fluid reaction pathways below venting areas. In particular, the existence of sulfur-bearing fluids seems to enhance metal mobility at depth. The percolation of such fluids toward the surface can lead to abundant magnetite precipitation and the formation of strong magnetic anomalies under active hydrothermal fields (e.g., Rainbow, Ashadzé; Sztikar et al., 2014), possibly equivalent to magnetite and chromite deposits observed in ophiolites (e.g., Toffolo et al., 2017; Hodel et al., 2017).

Acknowledgements

This research was supported by the F.N.R.S (Fond National de la Recherche Scientifique, Belgium) n°1.B.403.17F to BD. BD acknowledges his F.R.S.-F.N.R.S. research fellowship (Chargé de recherche). IRC acknowledges research fellowship SFRH/BSAB/135094/2017 from FCT – Fundação para a Ciência e Tecnologia (Portugal). The authors wish to thank J. De Jong (ULB) for technical support during MC-ICP-MS analyses. BD also acknowledges P. Sossi (IPG, Paris) for helpful discussions and providing access to Balmuccia data. We thank F. Klein and two anonymous reviewers for critical comments on earlier version of this article, and careful editorial handling by D. Vance.

Appendix A. Supplementary material

Supplementary material related to this article can be found online at <https://doi.org/10.1016/j.epsl.2018.09.009>.

References

- Allen, D.E., Seyfried, W.E., 2004. Serpentinization and heat generation: constraints from Lost City and Rainbow hydrothermal systems. *Geochim. Cosmochim. Acta* 68, 1347–1354. <https://doi.org/10.1016/j.gca.2003.09.003>.
- Alt, J., Shanks, W.C.S., 2003. Serpentinization of abyssal peridotites from the MARK area, Mid-Atlantic Ridge: sulfur geochemistry and reaction modeling. *Geochim. Cosmochim. Acta* 67, 641–653.
- Andreani, M., Escartin, J., Delacour, A., Ildefonse, B., Godard, M., Dymont, J., Fallick, A.E., Fouquet, Y., 2014. Tectonic structure, lithology, and hydrothermal signature of the rainbow massif (Mid-Atlantic Ridge 36°14'N). *Geochim. Geophys. Geosyst.* 15, 3543–3571. <https://doi.org/10.1002/2014GC005269>.
- Andreani, M., Muñoz, M., Marcaillou, C., Delacour, A., 2013. μXANES study of iron redox state in serpentine during oceanic serpentinization. *Lithos* 178, 70–83. <https://doi.org/10.1016/j.lithos.2013.04.008>.
- Baker, E.T., Edmonds, H.N., Michael, P.J., Bach, W., Dick, H.J.B., Snow, J.E., Walker, S.L., Banerjee, N.R., Langmuir, C.H., 2004. Hydrothermal venting in magma deserts: the ultraslow-spreading Gakkel and Southwest Indian Ridges. *Geochim. Geophys. Geosyst.* 5. <https://doi.org/10.1029/2004GC000712>.
- Beard, B.L., Johnson, C.M., Von Damm, K.L., Poulson, R.L., 2003. Iron isotope constraints on Fe cycling and mass balance in oxygenated Earth oceans. *Geology* 31, 629–632. [https://doi.org/10.1130/0091-7613\(2003\)031<0629:IIOCFC>2.0.CO;2](https://doi.org/10.1130/0091-7613(2003)031<0629:IIOCFC>2.0.CO;2).
- Blanchard, M., Poitrasson, F., Méheut, M., Lazzeri, M., Mauri, F., Balan, E., 2009. Iron isotope fractionation between pyrite (FeS_2), hematite (Fe_2O_3) and siderite (FeCO_3): a first-principles density functional theory study. *Geochim. Cosmochim. Acta* 73, 6565–6578. <https://doi.org/10.1016/j.gca.2009.07.034>.
- Bonnemains, D., Carlut, J., Escartin, J., Mével, C., Andreani, M., Debret, B., 2016. Magnetic signatures of serpentinization at ophiolite complexes. *Geochim. Geophys. Geosyst.* 17, 2969–2986. <https://doi.org/10.1002/2016GC006321>.
- Canales, J.P., Dunn, R.A., Arai, R., Sohn, R.A., 2017. Seismic imaging of magma sills beneath an ultramafic-hosted hydrothermal system. *Geology* 45, 451–454. <https://doi.org/10.1130/G38795.1>.
- Charlou, J., Donval, J., Fouquet, Y., Jean-Baptiste, P., Holm, N., 2002. Geochemistry of high H_2 and CH_4 vent fluids issuing from ultramafic rocks at the Rainbow hydrothermal field (36°14'N, MAR). *Chem. Geol.* 191, 345–359. [https://doi.org/10.1016/S0009-2541\(02\)00134-1](https://doi.org/10.1016/S0009-2541(02)00134-1).
- Craddock, P.R., Warren, J.M., Dauphas, N., 2013. Abyssal peridotites reveal the near-chondritic Fe isotopic composition of the Earth. *Earth Planet. Sci. Lett.* 365, 63–76. <https://doi.org/10.1016/j.epsl.2013.01.011>.
- Debret, B., Andreani, M., Delacour, A., Rouméjon, S., Trcera, N., Williams, H., 2017. Assessing sulfur redox state and distribution in abyssal serpentinites using XANES spectroscopy. *Earth Planet. Sci. Lett.* 466, 1–11. <https://doi.org/10.1016/j.epsl.2017.02.029>.
- Debret, B., Andreani, M., Godard, M., Nicollet, C., Schwartz, S., Lafay, R., 2013. Trace element behavior during serpentinization/de-serpentinization of an eclogitized oceanic lithosphere: a LA-ICPMS study of the Lanzo ultramafic massif (Western Alps). *Chem. Geol.* 357, 117–133. <https://doi.org/10.1016/j.chemgeo.2013.08.025>.
- Debret, B., Millet, M.A., Pons, M.L., Bouilhol, P., Inglis, E., Williams, H., 2016. Isotopic evidence for iron mobility during subduction. *Geology* 44, 215–218. <https://doi.org/10.1130/G37565.1>.
- Delacour, A., Früh-Green, G.L., Bernasconi, S.M., Schaeffer, P., Kelley, D.S., 2008. Carbon geochemistry of serpentinites in the Lost City Hydrothermal System (30°N, MAR). *Geochim. Cosmochim. Acta* 72, 3681–3702. <https://doi.org/10.1016/j.gca.2008.04.039>.
- Doucet, L.S., Mattielli, N., Ionov, D.A., Debouge, W., Golovin, A.V., 2016. Zn isotopic heterogeneity in the mantle: a melting control? *Earth Planet. Sci. Lett.* 451, 232–240. <https://doi.org/10.1016/j.epsl.2016.06.040>.
- Douville, E., Charlou, J.L., Oelkers, E.H., Bienvenu, P., Jove Colon, C.F., Donval, J.P., Fouquet, Y., Prieur, D., Appriou, P., 2002. The rainbow vent fluids (36°14'N, MAR): the influence of ultramafic rocks and phase separation on trace metal content in Mid-Atlantic Ridge hydrothermal fluids. *Chem. Geol.* 184, 37–48.
- Ducher, M., Blanchard, M., Balan, E., 2016. Equilibrium zinc isotope fractionation in Zn-bearing minerals from first-principles calculations. *Chem. Geol.* 443, 87–96. <https://doi.org/10.1016/j.chemgeo.2016.09.016>.
- Dunn, R.A., Arai, R., Eason, D.E., Canales, J.P., Sohn, R.A., 2017. Three-dimensional seismic structure of the Mid-Atlantic Ridge: an investigation of tectonic, magmatic, and hydrothermal processes in the Rainbow Area. *J. Geophys. Res., Solid Earth* 122, 9580–9602. <https://doi.org/10.1002/2017JB015051>.
- Fouquet, Y., Cambon, P., Etoubleau, J., Charlou, J.L., Ondréas, H., Barriga, F.J.A.S., Cherkashov, G., Semkova, T., Poroshina, I., Bohn, M., Donval, J.P., Henry, K., Murphy, P., Rouxel, O., 2010. Geodiversity of hydrothermal processes along the Mid-Atlantic Ridge and ultramafic-hosted mineralization: a new type of Oceanic Cu–Zn–Co–Au volcanogenic massive sulfide deposit. In: *Diversity of Hydrothermal Systems on Slow Spreading Oceanic Ridges*, pp. 321–367.
- Fujii, T., Moynier, F., Blichert-Toft, J., Albarède, F., 2014. Density functional theory estimation of isotope fractionation of Fe, Ni, Cu, and Zn among species relevant to geochemical and biological environments. *Geochim. Cosmochim. Acta* 140, 553–576. <https://doi.org/10.1016/j.gca.2014.05.051>.
- Godard, M., Lagabrielle, Y., Alard, O., Harvey, J., 2008. Geochemistry of the highly depleted peridotites drilled at ODP Sites 1272 and 1274 (Fifteen-Twenty Fracture

- Zone, Mid-Atlantic Ridge): implications for mantle dynamics beneath a slow spreading ridge. *Earth Planet. Sci. Lett.* 267, 410–425.
- Guo, J., Griffin, W.L., O'Reilly, S.Y., 1999. Geochemistry and origin of sulphide minerals in mantle xenoliths: Qilin, Southeastern China. *J. Petrol.* 40, 1125–1149. <https://doi.org/10.1093/ptro/40.7.1125>.
- Hedenquist, J.W., Lowenstern, J.B., 1994. The role of magmas in the formation of hydrothermal ore deposits. *Nature* 370, 519–527. <https://doi.org/10.1038/370519a0>.
- Hodel, F., Macouin, M., Triantafyllou, A., Carlut, J., Berger, J., Rousse, S., Ennih, N., Trindade, R.I.F., 2017. Unusual massive magnetite veins and highly altered Cr-spinels as relics of a Cl-rich acidic hydrothermal event in Neoproterozoic serpentinites (Bou Azzer ophiolite, Anti-Atlas, Morocco). *Precambrian Res.* 300, 151–167. <https://doi.org/10.1016/j.precamres.2017.08.005>.
- Holm, N.G., Charlou, J.L., 2001. Initial indications of abiotic formation of hydrocarbons in the Rainbow ultramafic hydrothermal system, Mid-Atlantic Ridge. *Earth Planet. Sci. Lett.* 191, 1–8.
- Ikehata, K., Hirata, T., 2012. Copper isotope characteristics of copper-rich minerals from the horoman peridotite complex, Hokkaido, Northern Japan. *Econ. Geol.* 107, 1489–1497. <https://doi.org/10.2113/econgeo.107.7.1489>.
- Jagoutz, E., Palme, H., Baddenhausen, H., Blum, K., Cendales, M., Dreibus, G., Spettel, B., Lorenz, V., Wänke, H., 1979. The abundances of major, minor and trace elements in the earth's mantle as derived from primitive ultramafic nodules. In: *Lunar and Planetary Science Conference, 10th, Proceedings, vol. 2 (A80-23617 08-91)*. Houston, Tex., March 19–23, 1979. Pergamon Press, Inc., New York, pp. 2031–2050.
- Kelley, D.S., Karson, J.A., Blackman, D.K., Fruh-Green, G.L., Butterfield, D.A., Lilley, M.D., Olson, E.J., Schrenk, M.O., Roe, K.K., Lebon, G.T., Rivizzigno, P., 2001. An off-axis hydrothermal vent field near the Mid-Atlantic Ridge at 30°N. *Nature* 412, 145–149. <https://doi.org/10.1038/35084000>.
- Klein, F., Bach, W., Humphris, S.E., Kahl, W.A., Jöns, N., Moskowicz, B., Berquó, T.S., 2014. Magnetite in seafloor serpentinite—some like it hot. *Geology* 42, 135–138. <https://doi.org/10.1130/G35068.1>.
- Maréchal, C.N., Télouk, P., Albarède, F., 1999. Precise analysis of copper and zinc isotopic compositions by plasma-source mass spectrometry. *Chem. Geol.* 156, 251–273. [https://doi.org/10.1016/S0009-2541\(98\)00191-0](https://doi.org/10.1016/S0009-2541(98)00191-0).
- Marques, A.F.A., Barriga, F., Chavagnac, V., Fouquet, Y., 2006. Mineralogy, geochemistry, and Nd isotope composition of the Rainbow hydrothermal field, Mid-Atlantic Ridge. *Miner. Depos.* 41, 52–67. <https://doi.org/10.1007/s00126-005-0040-8>.
- Marques, A.F.A., Barriga, F., Scott, S.D., 2007. Sulfide mineralization in an ultramafic-rock hosted seafloor hydrothermal system: from serpentinization to the formation of Cu–Zn–(Co)-rich massive sulfides. *Mar. Geol.* 245, 20–39. <https://doi.org/10.1016/j.margeo.2007.05.007>.
- McDonough, W., Sun, S.S., 1995. The composition of the earth. *Chem. Geol.* 120, 223–253.
- Moynier, F., Vance, D., Fujii, T., Savage, P., 2017. The isotope geochemistry of zinc and copper. *Rev. Mineral. Geochem.* 82, 543–600. <https://doi.org/10.2138/rmg.2017.82.13>.
- Ohara, Y., Reagan, M.K., Fujikura, K., Watanabe, H., Michibayashi, K., Ishii, T., Stern, R.J., Pujana, I., Martinez, F., Girard, G., Ribeiro, J., Brounce, M., Komori, N., Kino, M., 2012. A serpentinite-hosted ecosystem in the Southern Mariana Forearc. *Proc. Natl. Acad. Sci.* 109, 2831–2835. <https://doi.org/10.1073/pnas.1112005109>.
- Othman, B.D., Luckck, J.M., Bodinier, J.L., Arndt, N.T., Albarède, F., 2006. Cu–Zn isotopic variations in the Earth's mantle. *Geochim. Cosmochim. Acta* 70, A46.
- Paulick, H., Bach, W., Godard, M., Hoog, C.-J., Suhr, G., Harvey, J., 2006. Geochemistry of abyssal peridotites (Mid-Atlantic Ridge, 15–20°N, ODP Leg 209): implications for fluid/rock interaction in slow spreading environments. *Chem. Geol.* 234, 179–210.
- Petit, J.C.J., de Jong, J., Chou, L., Mattioli, N., 2008. Development of Cu and Zn isotope MC-ICP-MS measurements: application to suspended particulate matter and sediments from the scheldt estuary. *Geostand. Geoanal. Res.* 32, 149–166. <https://doi.org/10.1111/j.1751-908X.2008.00867.x>.
- Pogge von Strandmann, P.A., Dohmen, R., Marschall, H.R., Schumacher, J.C., Elliott, T., 2015. Extreme magnesium isotope fractionation at outcrop scale records the mechanism and rate at which reaction fronts advance. *J. Petrol.* 56, 33–58.
- Pons, M.L., Debret, B., Bouilhol, P., Delacour, A., Williams, H., 2016. Zinc isotope evidence for sulfate-rich fluid transfer across subduction zones. *Nat. Commun.* 7, 13794. <https://doi.org/10.1038/ncomms13794>.
- Pons, M.L., Quitté, G., Fujii, T., Rosing, M.T., Reynard, B., Moynier, F., Douchet, C., Albarède, F., 2011. Early archean serpentine mud volcanoes at Isua, Greenland, as a niche for early life. *Proc. Natl. Acad. Sci. USA* 108, 17639–17643.
- Ribeiro da Costa, I., 2005. Serpentinization on the Mid-Atlantic Ridge: The Rainbow, Saldanha and Menez Hom Sites. PhD thesis. University of Lisbon. 444 p.
- Rouméjon, S., Cannat, M., Agrinier, P., Godard, M., Andreani, M., 2015. Serpentinization and fluid pathways in tectonically exhumed peridotites from the Southwest Indian Ridge (62–65E). *J. Petrol.* 56, 703–734.
- Rouxel, O., Dobbek, N., Ludden, J., Fouquet, Y., 2003. Iron isotope fractionation during oceanic crust alteration. *Chem. Geol.* 202, 155–182. <https://doi.org/10.1016/j.chemgeo.2003.08.011>.
- Rouxel, O., Fouquet, Y., Ludden, J.N., 2004. Copper isotope systematics of the Lucky Strike, Rainbow, and Logatchev sea-floor hydrothermal fields on the Mid-Atlantic Ridge. *Econ. Geol.* 99, 585–600. <https://doi.org/10.2113/gsecongeo.99.3.585>.
- Rouxel, O., Shanks, W.C., Bach, W., Edwards, K.J., 2008. Integrated Fe- and S-isotope study of seafloor hydrothermal vents at East Pacific Rise 9–10°N. *Chem. Geol.* 252, 214–227. <https://doi.org/10.1016/j.chemgeo.2008.03.009>.
- Savage, P.S., Moynier, F., Chen, H., Shofner, G., Siebert, J., Badro, J., Puchtel, I.S., 2015. Copper isotope evidence for large-scale sulphide fractionation during Earth's differentiation. *Geochem. Perspect. Lett.*, 53–64. <https://doi.org/10.7185/geochemlett.1506>.
- Scott, S.R., Sims, K.W.W., Frost, B.R., Kelemen, P.B., Evans, K.A., Swapp, S.M., 2017. On the hydration of olivine in ultramafic rocks: implications from Fe isotopes in serpentinites. *Geochim. Cosmochim. Acta* 215, 105–121. <https://doi.org/10.1016/j.gca.2017.07.011>.
- Severmann, S., Johnson, C.M., Beard, B.L., German, C.R., Edmonds, H.N., Chiba, H., Green, D.R.H., 2004. The effect of plume processes on the Fe isotope composition of hydrothermally derived Fe in the deep ocean as inferred from the Rainbow vent site, Mid-Atlantic Ridge, 36°14'N. *Earth Planet. Sci. Lett.* 225, 63–76. <https://doi.org/10.1016/j.epsl.2004.06.001>.
- Sossi, P.A., Halverson, G.P., Nebel, O., Eggins, S.M., 2015. Combined separation of Cu, Fe and Zn from rock matrices and improved analytical protocols for stable isotope determination. *Geostand. Geoanal. Res.* 39, 129–149. <https://doi.org/10.1111/j.1751-908X.2014.00298.x>.
- Sossi, P.A., Nebel, O., O'Neill, H.S.C., Moynier, F., 2018. Zinc isotope composition of the Earth and its behaviour during planetary accretion. *Chem. Geol.* 477, 73–84. <https://doi.org/10.1016/j.chemgeo.2017.12.006>.
- Syverton, D.D., Pester, N.J., Craddock, P.R., Seyfried, W.E., 2014. Fe isotope fractionation during phase separation in the NaCl–H₂O system: an experimental study with implications for seafloor hydrothermal vents. *Earth Planet. Sci. Lett.* 406, 223–232. <https://doi.org/10.1016/j.epsl.2014.09.020>.
- Szitar, F., Dymant, J., Fouquet, Y., Honsho, C., Horen, H., 2014. The magnetic signature of ultramafic-hosted hydrothermal sites. *Geology* 42, 715–718. <https://doi.org/10.1130/G35729.1>.
- Takazawa, E., Frey, F.A., Shimizu, N., Obata, M., 2000. Whole rock compositional variations in an upper mantle peridotite (Horoman, Hokkaido, Japan): are they consistent with a partial melting process? *Geochim. Cosmochim. Acta* 64, 695–716.
- Telus, M., Dauphas, N., Moynier, F., Tissot, F.L.H., Teng, F.Z., Nabelek, I., Craddock, P.R., Groat, L.A., 2012. Iron, zinc, magnesium and uranium isotopic fractionation during continental crust differentiation: the tale from migmatites, granitoids, and pegmatites. *Geochim. Cosmochim. Acta* 97, 247–265.
- Toffolo, L., Nimis, P., Martin, S., Tumiati, S., Bach, W., 2017. The Cogne magnetite deposit (Western Alps, Italy): a Late Jurassic seafloor ultramafic-hosted hydrothermal system? *Ore Geol. Rev.* 83, 103–126.
- Wang, Z.Z., Liu, S.A., Liu, J., Huang, J., Xiao, Y., Chu, Z.Y., Zhao, X.M., Tang, L., 2017. Zinc isotope fractionation during mantle melting and constraints on the Zn isotope composition of Earth's upper mantle. *Geochim. Cosmochim. Acta* 198, 151–167. <https://doi.org/10.1016/j.gca.2016.11.014>.
- Williams, H.M., Peslier, A.H., McCammon, C., Halliday, A.N., Levasseur, S., Teutsch, N., Burg, J.P., 2005. Systematic iron isotope variations in mantle rocks and minerals: the effects of partial melting and oxygen fugacity. *Earth Planet. Sci. Lett.* 235, 435–452. <https://doi.org/10.1016/j.epsl.2005.04.020>.